Metals and Materials International (2020) 26:69–74
https://doi.org/10.1007/s12540-019-00302-6

Anelastic and Microplastic Damping of an Mg–Zn–Y–Al Alloy

Diqing Wan[1] · Jiajun Hu[1] · Yinglin Hu[1] · Houbin Wang[1]

Received: 3 March 2019 / Accepted: 14 May 2019 / Published online: 4 June 2019

Abstract
In this study, the $Mg_{97}Zn_1Y_2$–Al alloy was selected as a high damping material, anelastic and microplastic damping were analyzed by studying strain amplitude-dependent damping curves of the alloy. The C_1 and C_2 values of the Granato–Lücke (G–L) model, the theoretical basis of anelastic damping, can be calculated for each alloy, then, the corresponding numbers of strong and weak pinners are deduced. However, since the occurrence of microplastic damping in a high strain amplitude cannot be explained by the G–L model, a new microplastic damping theory was introduced, by comparing the activation volume of the material dislocation slip, the microplastic damping capacity of the $Mg_{97}Zn_1Y_2$–xwt%Al (x = 0.3, 1, 3) alloys at the microplastic stage are compared. The elastic and plastic deformation of the materials could be sensitively reflected by studying the damping behavior of these two stages.

Keywords Mg–Zn–Y–Al alloy · Strain amplitude · Anelastic damping · Microplastic damping

1 Introduction

With the rapid development of industrialization, the harm caused by noise and vibration to both machinery and human body has become a serious issue that cannot be ignored [1]. The application of damping materials is one of the methods to reduce such vibration and noise [2]. As early as in the 1950 s, Zener [3] published the renowned work about the elasticity and anelasticity of metals and people began to explore high-damping materials based on the anelastic theory. The study of the damping mechanism of metals in various states is crucial for developing high-performance metal-based materials.

In our previous study [4], the $Mg_{97}Zn_1Y_2$–xwt%Al (x = 0.3, 1, 3) alloy has been defined as a promising high-strength and high-damping magnesium alloy due to the presence of a long-period stacking ordered (LPSO) phase, which can balance its damping and mechanical properties. Therefore, in this work, the same alloy was selected to investigate the damping-strain amplitude dependence of high-damping Mg alloys in a wide range of strain amplitudes. This study could not only clarify the damping capacity of this material but also provide its damping response under different deformation states, through which its elastic and plastic deformation could be sensitively reflected.

According to the Granato–Lücke (G–L) model, the damping-strain amplitude curve of a material is usually divided into two segments [5, 6], the strain amplitude-independent segment and the strain amplitude-dependent one. However, some studies suggest that [7, 8] when the strain amplitude exceeds a certain value, this curve can no longer be explained by the classical G–L model. In this study, an Mg–Zn–Y–Al alloy was used as an example to explain the anelastic and microplastic damping in detail, and a model for describing the microplastic damping of magnesium alloys was introduced.

2 Experimental

$Mg_{97}Zn_1Y_2$–xwt%Al alloys were prepared by conventional casting method. Pure Mg (99.9% purity), pure Zn (99.9% purity), Mg–25wt%Y binary alloy, and high-purity Al flakes were selected as the raw materials. The traditional casting process was used to smelt in XMT well resistance furnace under the condition of 720 °C. The molten metal was pouring into the metal mold for air cooling. The microstructure of the specimens was observed by an optical microscope (COOLPIX-4500) and a scanning electron

✉ Diqing Wan
divadwan@tom.com; divadwan@163.com

[1] School of Materials Science and Engineering, East China Jiaotong University, Nanchang 330013, China

microscope (SEM) with an energy dispersive spectroscopy (EDS) analyzer (JSM 6701F). The damping performance was tested by dynamic mechanical thermal analysis (DMA Q800). The temperature of the strain amplitude dependent damping test is at room temperature, and the vibration frequency is 1 Hz. In order to facilitate observation, the strain amplitude is increased as much as possible in the damping test, the strain amplitude interval is 1×10^{-3} to 4×10^{-3}, which is covered over anelastic and microplastic zone. The test-pieces for damping were machined with dimension of 50 mm × 5 mm × 1 mm on electric spark cutter and properly installed in the DMA testing head, was constrained at each end by a clamping bar arrangement with one end fixed to a rigid frame and the other end driven by an electromagnetic vibrator via a composite drive shaft. The resulting sinusoidal force and deflection data were recorded and analyzed by modulus. The internal friction value of material in the damping-strain spectrum was evaluated by loss tangent (tanδ), which can be expressed by Q^{-1}.

3 Results and Discussion

3.1 Microstructure

Figure 1a shows the optical microscopy images of the $Mg_{97}Zn_1Y_2$ alloy, which is mainly revealed a coarse dendrite structure and the uneven distribution of a secondary phase, while the morphologies resulting from the Al addition are displayed in Fig. 1b–d. When the Al content added was 0.3 wt%, the morphology of the secondary phase did not change significantly; however, the increasing of its content hindered the dendrite structure growth, refined the dendrite size to a certain extent, and promoted the generation and even distribution of the secondary phase [4].

Figure 2 and Table 1 show the SEM images and EDS results of the $Mg_{97}Zn_1Y_2$–xwt%Al alloy. The 001 point was located on the dendrite structure where the Zn/Y ratio was close to 1:1, possibly corresponding to an LPSO

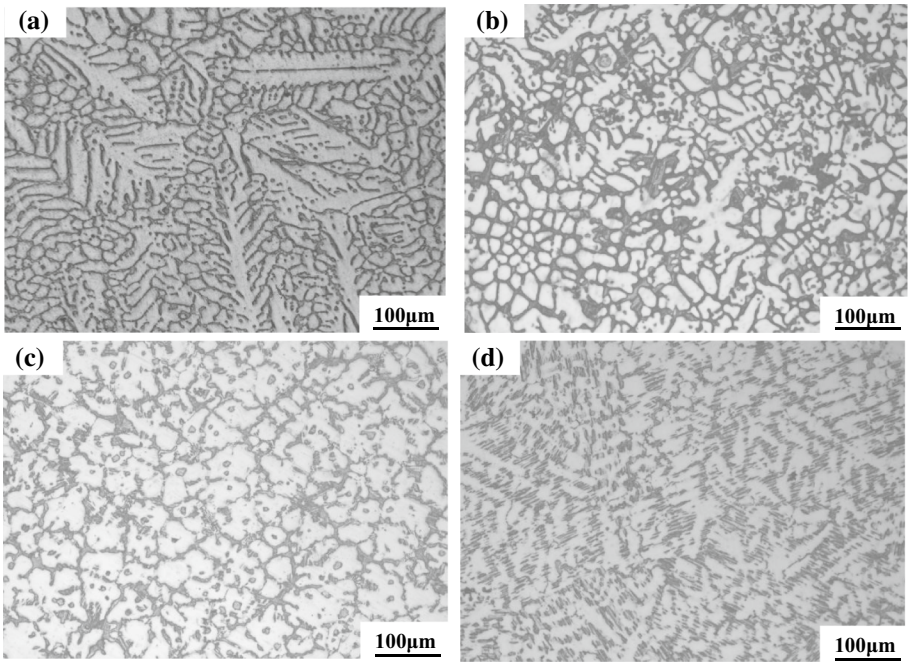

Fig. 1 Microstructure of cast $Mg_{97}Zn_1Y_2$–Al_x alloy under optical microscope. **a** x = 0; **b** x = 0.3; **c** x = 1; **d** x = 3

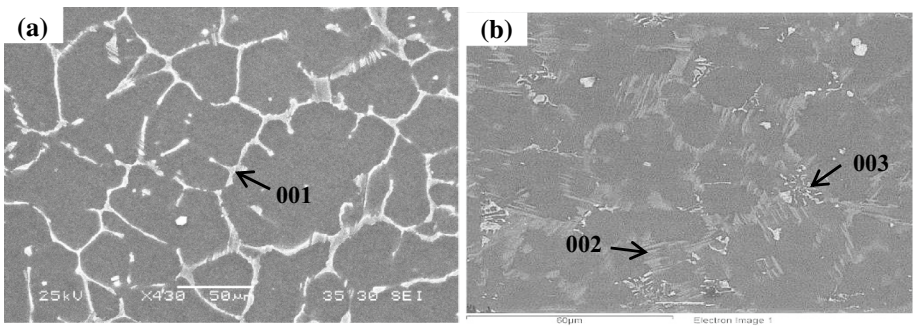

Fig. 2 Microstructure of as-cast $Mg_{97}Zn_1Y_2$–Al_x under scanning electron microscope (SEM). **a** x = 0; **b** x = 1

Table 1 The energy spectrum analysis of alloy components

Spot	Mg (at%)	Zn (at%)	Y (at%)	Al (at%)
001	84.84	7.66	7.50	0
002	87.82	5.11	7.07	0
003	58.26	5.29	0	36.45

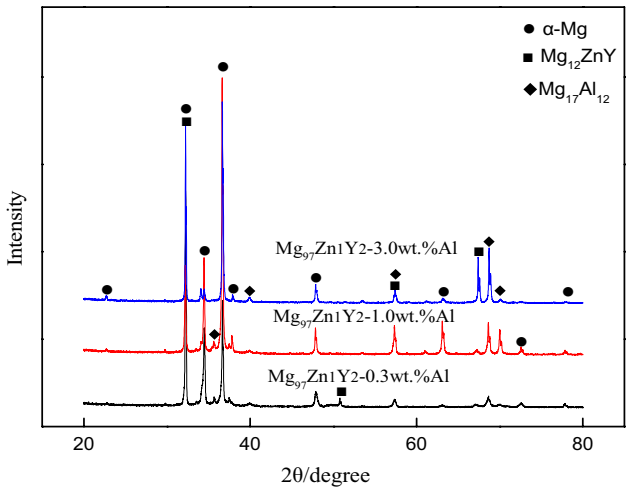

Fig. 3 X-ray diffraction (XRD) analysis of $Mg_{97}Zn_1Y_2$–Al_x alloy

phase. For the Al content of 1.0 wt%, the alloy components at the 002 point were similar to those at the 001 one, while the 003 point stood out, according to the Al content, the phase at this point was probably an Al-containing phase. As shown in Fig. 2b, this phase exhibited a network-like distribution, which normally hinders grain growth during crystallization. According to the Mg–Al phase diagram [9], during the crystallization, the eutectic reaction $L \rightarrow \alpha\text{-Mg} + \beta\text{-}Mg_{17}Al_{12}$ occurs at the eutectic temperature (437 °C); hence, the above-mentioned Al-containing phase at the 003 point could be $Mg_{17}Al_{12}$. The diffraction peaks were observed in the XRD analysis (Fig. 3) suggested that the $Mg_{97}Zn_1Y_2$–xwt%Al alloy consists of α-Mg, $Mg_{12}ZnY$ phase (LPSO), and $Mg_{17}Al_{12}$ phase. Thus, the dendrite structures observed at the 001 and 002 points belonged both to the $Mg_{12}ZnY$ phase, while the network structure at the 003 point probably corresponded to the $Mg_{17}Al_{12}$ one.

3.2 Damping Analysis of Anelasticity

Magnesium presents the highest damping properties among light metals, which is typical dislocation damping mechanism material [10–13]. Dislocation damping is mainly caused by the dislocation movement among defects under stress and its theoretical model has been proposed by Granato and Lücke [14]. According to this G–L model, the damping of materials can be divided into two stages, observed at two different strain amplitude ranges: (1) at a low strain amplitude range, the dislocation lines move around weak pinners and the damping, denoted by Q_0^{-1} at this stage, is independent or weakly dependent of the strain amplitude; (2) at a strain amplitude greater than the critical strain amplitude, the dislocations slip between strong pinners and the damping value, now denoted by Q_h^{-1}, increases with the strain amplitude. Therefore, the damping value can be expressed as follows [15, 16]:

$$Q^{-1} = Q_0^{-1} + Q_h^{-1} \tag{1}$$

Q_0^{-1} and Q_h^{-1} are obtained by

$$Q_0^{-1} = \frac{\rho B L_c^4 \omega}{36 G b^2} \tag{2}$$

and

$$Q_h^{-1} = \frac{C_1}{\varepsilon}\exp\left(-\frac{C_2}{\varepsilon}\right) \tag{3}$$

where $C_1 = \frac{\rho F_B L_N^3}{6bEL_C^2}$, $C_2 = \frac{F_B}{bEL_C}$, ρ is the movable dislocation density, b is the Berkeley vector of a dislocation, ω is the corner frequency, B is a constant, it is a movable dislocation density, L_C and L_N are the distances between adjacent weak and strong pinners, respectively, F_B is the point force between defects and dislocations, E is the elastic modulus, and G is the shear modulus. Equation (3) can be also expressed as

$$\ln(Q_h^{-1} \cdot \varepsilon) = \ln C_1 - C_2/\varepsilon \tag{4}$$

The $\ln(Q_h^{-1} \cdot \varepsilon) - 1/\varepsilon$ curve shown in Fig. 4a was plotted according to Eq. (4); it is called G–L plot and is often used as an applicability criterion for the G–L model.

Figure 4 shows the G–L curve of the $Mg_{97}Zn_1Y_2$–xwt%Al alloy. In the first stage ($\varepsilon < \varepsilon_{cr1}$), the damping value changed slightly; according to the G–L model, since the dislocation line was pinned by the weak pinners and could only perform reciprocating motion between them, it was less affected by the strain amplitude. In the second strain range ($\varepsilon_{cr1} < \varepsilon < \varepsilon_{cr2}$, Fig. 4b), the G–L curve was clearly a straight line and the damping value at this stage could be explained by the dislocation damping mechanism and yield to the G–L dislocation model. In this range, with the increase of the strain amplitude, an increasing number of dislocation lines that break away from the weak pinners and bowed out between with the strong pinners. This suggests that the damping capacities strongly depend on the strain amplitude. When the strain amplitude exceeded the second critical strain amplitude (ε_{cr2}), the G–L curve deviated from the straight line and the dislocation lines started break away from the strong pinners; this is considered the beginning of the microplastic deformation of the material.

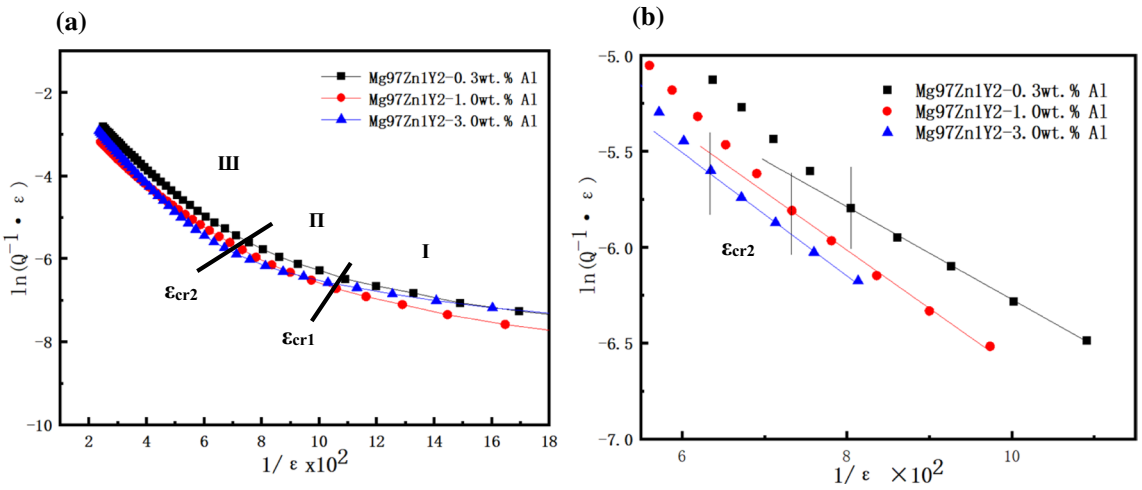

Fig. 4 The G–L curve of $Mg_{97}Zn_1Y_2$–Al_x alloy. **a** The range of the whole strain amplitude; **b** $\varepsilon_{cr1} < \varepsilon < \varepsilon_{cr2}$

Table 2 C_1, C_2 value and critical strain amplitude of $Mg_{97}Zn_1Y_2$–Al_x alloy

	$Mg_{97}Zn_1Y_2$–0.3wt.Al	$Mg_{97}Zn_1Y_2$–1.0wt.Al	$Mg_{97}Zn_1Y_2$–3.0wt.Al
$C_1 \times 10^2$	2.17	2.75	2.80
C_2	0.244	0.302	0.322
$\varepsilon_{cr1} \times 10^2$	0.092	0.103	0.122
$\varepsilon_{cr2} \times 10^2$	0.124	0.136	0.157

According to Eq. (4), the line slope is $-C_2$, the intersection of the y-axis is $\ln C_1$, the specific numerical results of C_1 and C_2 were calculated, as listed in Table 2. A smaller L_C value implies a larger number of weak pinners in the dislocation and the C_2 value is proportional to the latter; therefore, C_2 is inversely proportional to L_C. The C_2 value increases with the Al content, meaning that also the number of weak pinners increases with it. Aluminum has a maximum solubility of 12.5% in Mg [17]; with the Al addition, more solute atoms are solid-solutioned into the Mg matrix, resulting in more weak pinners on the dislocation line, which consecutively requires a greater strain to be removed from them. This conclusion can be supported by Table 2 that shows the increase of ε_{cr1} with the Al addition.

According to Table 2, C_1 is proportional to the Al content and $\rho L_N^3 / L_C^2$. Based on the alloy microstructure shown in Fig. 1, as the Al content increases, more secondary phase ($Mg_{17}Al_{12}$), which corresponds to the strong pinners on the dislocation line, is formed in the matrix. Therefore, as the Al content increases, the number of strong pinners increases, while the L_N value decreases. Figure 1 also shows that an increase in the Al content further refined the microstructure and generated more interfaces. These factors improve the mechanical properties of the material [4], hence, its microplastic deformation requires a greater strain amplitude, as supported by the results in Table 2. Trojanov et al. [18] reported that, due to the different thermal expansion coefficients between matrix and particles, the dislocation density at their interface is much larger than that in the matrix. Therefore, the formation of the secondary phase also increases the dislocation density of the material. Comprehensive consideration of the above analysis, the increase in C_1 value is in line with previous theories.

3.3 Damping in Microplastic Deformation

When the strain amplitude was greater than ε_{cr2}, the G–L curve clearly deviated from the straight line. Since this aspect cannot be explained by the G–L theory, a more appropriate theory for the microplastic deformation is required. Dislocation lines sweep a certain area and consume energy; when they get far from all the weak pinning points, the elastic energy consumed reaches the limit and the high-strain zone damping gets saturated [19, 20]. However, as the strain continues to increase, the material damping still rises. Mason [21] attributed this damping mechanism to the plastic deformation. At this stage, a larger strain causes significant microplastic deformations the material (generally referred to the plastic deformation before the macroscopic yield point of 0.2% [22–24]) and the dislocation line begins to get far from the strong pinners, producing damping associated with the microplastic deformation, which is denoted by Q_p^{-1}.

Penguin [25] proposed a model to explain the damping phenomenon associated with the microplastic deformation and the factors influencing the damping value at this stage, represented as follows:

$$Q_p^{-1} = \frac{A}{\varepsilon h} \exp(B\varepsilon - B\varepsilon_p), \tag{5}$$

$$A = \frac{2\rho bv}{\pi f} \exp\left(-\frac{Q}{KT}\right), \tag{6}$$

and

$$B = \alpha \frac{VG}{KT}, \tag{7}$$

where h is a constant, v is the eigenfrequency of the dislocation, ρ is the movable dislocation density, f is the test frequency, Q is the activation energy, α is the orientation factor, G is the shear modulus, ε_p is the strain amplitude at the beginning of the plastic damping, and V is the activation volume.

From Eq. (5), we obtain

$$\ln Q_p^{-1}\varepsilon = B\varepsilon + C \tag{8}$$

where $C = \ln A/h - B\varepsilon_p$

The microplastic damping curves were fitted according to Eq. (8) and that of the $Mg_{97}Zn_1Y_2$–xwt%Al alloy (Fig. 5) exhibited a clear turning point (ε_{cr3}). When the strain amplitude is greater than ε_{cr2}, the dislocation line begins to deviate from the equilibrium position. At this stage, the material undergoes microplastic deformation, with an associated microplastic damping (Q_p^{-1}).

On the other hand, with the strain amplitude increasingly, more movable dislocation sources inside the material are activated and, hence, Q_p^{-1} increases. According to Eq. (7), the slope of the curve is proportional to the activation volume of the material dislocation slip. As shown in Fig. 5, when the strain amplitude exceeded ε_{cr3}, the curve slope dropped significantly; in such cases, the material is usually deformed plastically by slippage, the dislocations on the same basal plant begin to entangle and accumulate, and the back stress generated by this dislocation accumulation

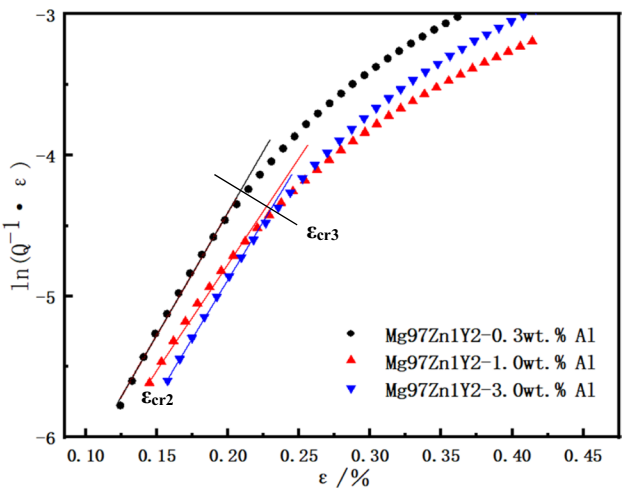

Fig. 5 The microplastic damping curve of $Mg_{97}Zn_1Y_2$–Al_x alloy

Table 3 The slope value and critical strain amplitude of microplastic damping curve of $Mg_{97}Zn_1Y_2$–Al_x alloy

Alloy	$\varepsilon_{cr3}\times10^2$	$K\times10^2$
$Mg_{97}Zn_1Y_2$–0.3wt%Al	0.206	17.39
$Mg_{97}Zn_1Y_2$–1.0wt%Al	0.212	14.97
$Mg_{97}Zn_1Y_2$–3.0wt%Al	0.235	16.25

makes the activation of dislocation sources more and more difficult [23]. The quenching and entanglement of the dislocations lead to fewer and fewer movable dislocations within the grains; therefore, above ε_{cr3}, the material hardens and the volume activated by the dislocation slipping decreases.

Table 3 shows the slopes and critical strain amplitudes of the damping curves for the microplastic deformation of the various alloys tested; the one with 0.3 wt% of Al exhibited the maximum V and minimum ε_{cr3}, corresponding to the damping curve at the high-strain amplitude stage, where its damping value was higher than that of the other alloys. This happened because this alloy had fewer pinners than the others, so that the dislocations were more easily removed, hence, the activation volume of the dislocation slipping was larger. Furthermore, the Al addition refines the grain size, forming the secondary phase and significantly improving the mechanical properties of the alloy, which leads to materials more difficult to plastically deform; therefore, with increasing the Al addition, ε_{cr3} increases, which is consistent with the results shown in Table 3. When the alloy is added with 3 wt% of Al at the high-strain amplitude, the damping is greater than that for the one added with 1 wt% of it. This may be due to the effect of the secondary phase ($Mg_{17}Al_{12}$) on the damping mechanism. Zhang et al. [26] reported that the secondary phase influences the damping behaviors of alloys via some possible mechanisms. One of them is the energy dissipation by the interfaces between primary and secondary phases under cyclic loading, which usually occurs at the weaker interface band. This mechanism of the $Mg_{97}Zn_1Y_2$–xwt%Al alloy could be considered, if the interface significantly causes energy dissipation, the alloy with more secondary phase will exhibits higher damping, which is consistent with the experimental results. Therefore, the increase in alloy damping with the Al content is mainly due to the increase in interface damping.

4 Conclusions

1. In the anelastic stage of damping, the classical G–L model can be applied and the mechanism of dislocation damping is dominant. The numbers of weak and strong pinners and the moveable dislocation density in the $Mg_{97}Zn_1Y_2$–xwt%Al alloy increase with the Al con-

tent and the dislocation lines require greater strain to be moved away from the weak pinners.

2. In the microplastic stage of damping, the G–L model no longer applies, hence, a new dislocation damping model has been proposed. Based on this new model, the relative activation volume of the dislocation slipping for the microplastic-dependent damping can be obtained from the slope of the straight line.

Acknowledgements This work was financially supported by the National Natural Science Foundation of China (51665012) and Supported by Jiangxi province Science Foundation for Outstanding Scholarship (20171BCB23061, 2018ACB21020).

References

1. J.B. Yao, H. Xia, N. Zhan, Procedia Eng. **199**, 2747–2752 (2017)
2. R. Schaller, J. Alloys Compd. **355**, 131–135 (2003)
3. C. Zener, *Elasticity and Anelasticity of Metals* (University of Chicago Press, Chicago, 1948)
4. D. Wan, H.B. Wang, S.T. Ye, Y.L. Hu, L.L. Li, J. Alloys Compd. **782**, 421–426 (2019)
5. A. Granato, K. Lücke, J. Appl. Phys. **27**, 583–593 (1956)
6. A. Granato, K. Lücke, J. Appl. Phys. **27**, 789–805 (1956)
7. C.F. Burdett, Philos. Mag. **24**, 1459–1464 (1971)
8. R. González-Martínez, J. Göken, D. Letzig, J. Timmerberg, K. Steinhoff, K.U. Kainer, Acta Metall. Sin. **20**, 235–240 (2007)
9. C.M. Liu, X.R. Zhu, H.T. Zhao, *The Magnesium Alloys Phase Diagram* (University of Central South Press, China, 2006), p. 4
10. M.R. Barnett, Z. Keshavarz, A.G. Beer, X. Ma, Acta Mater. **56**, 5–15 (2008)
11. B. Beausir, S. Biswas, D.I. Kim, L. Toth, S. Suwas, Acta Mater. **57**, 5061–5077 (2009)
12. S. Biswas, S.S. Dhinwal, S. Suwas, Acta Mater. **58**, 3247–3261 (2010)
13. D.L. Yin, J.T. Wang, J.Q. Liu, X. Zhao, J. Alloys Compd. **478**, 789–795 (2009)
14. D. Wan, J. Wang, Rare Met. Mater. Eng. **46**, 2790–2793 (2017)
15. T. Motoyama, H. Watanabe, N. Ikeo, Mater. Lett. **201**, 144–147 (2017)
16. H. Somekawa, H. Watanabe, D.A. Basha, Scr. Mater. **129**, 35–38 (2017)
17. D. Liu, J. Song, B. Jiang, J. Alloys Compd. **737**, 263–270 (2017)
18. Z. Trojanov, W. Riehemann, H. Ferkel, P. Lukáč, J. Alloys Compd. **310**, 396–399 (2000)
19. O.A. Lambri, W. Riehemann, E.J. Lucioni, R.E. Bolmaro, Mater. Sci. Eng. A **442**, 476–479 (2006)
20. L.H. Liao, X.Q. Zhang, X.F. Li, H.W. Wang, N.H. Ma, Mater. Lett. **61**, 231–234 (2007)
21. W.P. Mason, *Resonance and Relaxation in Metals* (Plenum Press, New York, 1964), p. 247
22. J.M. Roberts, N. Brown, Trans. Metall. Soc. AIME **218**, 454–463 (1960)
23. D.A. Thomas, B.L. Averbach, Acta Metall. **7**, 69–75 (1959)
24. N. Brown, K.F. Lukens, Acta Metall. **9**, 106–111 (1961)
25. P. Peguin, J. Perez, P. Gobin, Trans. Metall. Soc. AIME **239**, 438–450 (1967)
26. J.M. Zhang, R.J. Perez, C.R. Wong, Mater. Sci. Eng. R **13**, 325–389 (1994)